ROYAL SOCIETY
OF CHEMISTRY

Check for updates

Sustainable valorisation of wastewater sludge into activated carbon for permanganate adsorption and reuse in supercapacitors

Mojeed O. Bello, [ID] * Thabo T. I. Nkambule [ID] and Moshawe J. Madito [ID] *

Wastewater sludge from treatment processes was valorised into activated carbon *via* carbonisation, followed by chemical activation using orthophosphoric acid (H_3PO_4) and tagged H-WSAC. The H-WSAC was employed as an adsorbent in the removal of permanganate ions (MnO_4^-) from water, achieving a maximum adsorption capacity of 78.36 mg g^{-1} at an initial concentration of 100 mg L^{-1}. Adsorption kinetics followed a pseudo-second-order model ($R^2 = 0.9754$), indicating chemisorption, and equilibrium data fitted the Langmuir isotherm ($R^2 = 0.974$), suggesting monolayer adsorption. The physicochemical properties of pristine (H-WSAC) and spent (Mn-WSAC) adsorbents were characterised by Fourier-transform infrared spectroscopy, Raman spectroscopy, X-ray diffraction, scanning electron microscopy coupled with energy-dispersive X-ray spectroscopy, and transmission electron microscopy. The captured Mn species subsequently act as redox-active sites, facilitating the transition from water treatment to energy storage. The spent adsorbent, Mn-WSAC, was revalorised as an electrode material for supercapacitors. The symmetric supercapacitor using Mn-WSAC in a 1 M H_2SO_4 electrolyte exhibited a specific capacitance of 102 F g^{-1}, an energy density of 14.16 Wh kg^{-1}, and a power density of 1000 W kg^{-1} at a current density of 0.5 A g^{-1}, while retaining 83.15% of its initial capacitance over 15 000 cycles. This study offers a sustainable approach to wastewater sludge management by converting sludge into activated carbon for water purification and subsequent energy storage applications.

1 Introduction

Each year, an estimated 60 million tons of wastewater sludge is produced globally, highlighting a significant challenge in the circular economy where waste materials can become valuable resources. Permanganate ions (MnO_4^-), commonly encountered as potassium permanganate ($KMnO_4$), are potent oxidizing agents recognised for their strong oxidative capabilities.[1] This deep purple ion is extensively applied in various industrial and environmental contexts due to its efficacy and the benign nature of its reduced form, manganese dioxide (MnO_2).[2] Permanganate plays a critical role in water treatment processes, including disinfection, odour control, and removal of trace metals such as manganese and iron.[3] In addition to environmental applications, permanganate is utilised in organic synthesis, analytical testing, and fruit preservation by oxidising ethylene to delay ripening.[4,5] However, concentrations exceeding the World Health Organisation (WHO) permissible limit of 0.5 mg L^{-1} are toxic.[6] Exposure through splashing or ingestion can cause irritation to the skin and eyes, as well as liver and kidney damage. The health risk is notable, with typical

exposure scenarios including accidental spills and leaks. For instance, exposure to concentrations above the permissible limit can lead to acute health effects, while lower doses may accumulate over time. LD_{50} data further highlight the risks, as values for oral exposure in rats are around 1 g kg^{-1}.[7] A contrast between safe drinking-water guidelines and concentrations in real-world spill events underscores the importance of maintaining strict controls and highlights the need for effective removal of permanganate from contaminated water.

Adsorption technology in water treatment has been at the forefront as an efficient, environmentally friendly, and economically viable remediation process. A critical advantage of the adsorption process in water treatment is its ability to remove pollutants even when present at extremely low concentrations.[8] In view of this, the adsorption process can be employed in the cleanup of residual MnO_4^- from water. Various adsorbent materials, such as activated charcoal,[9] raw biomass,[10] polymer,[11] and activated carbon,[12,13] have been utilised in the removal of MnO_4^- from water. While adsorption is essential in the wastewater treatment process as a tertiary method, it is equally necessary to highlight the importance of the preliminary, primary, and secondary treatments.

Wastewater treatment plants produce biosolids, or sludge, as a byproduct.[14,15] The treatment process comprises five stages: preliminary, primary, secondary, tertiary, and sludge

Institute for Nanotechnology and Water Sustainability (iNanoWS), College of Science, Engineering and Technology, University of South Africa, Johannesburg 1710, South Africa. E-mail: bellomo@unisa.ac.za; maditmj@unisa.ac.za

management.[16] During the preliminary stage, physical processes remove large debris and waste.[17] Sludge forms during the primary and secondary stages through sedimentation and biological treatment.[16,18] Effective management of this sludge is addressed in the fifth stage, which includes stabilisation, thickening, dewatering, and drying to minimise environmental impact. Valorisation of sludge into useful products, such as activated carbon, biogas, and supplementary cementitious materials (SCMs), offers an alternative management strategy.[19–23] Several studies have reported the use of sludge-based precursors for activated carbon production. For example, activated carbon has been synthesised from wastewater sludge using zinc chloride (ZnCl$_2$) activation at 500 °C for two hours for phenol and carbon tetrachloride removal.[24] Similarly, chemical activation with potassium hydroxide (KOH) at 600 °C for two hours has produced activated carbon for heavy metal remediation.[25]

Despite the significant contribution and achievement made in the application of activated carbon in water treatment, the regeneration of spent activated carbon and other adsorbents demands high energy and requires expensive chemicals.[26] Also, the adsorption capacity of those that are regenerated is usually limited.[27] Therefore, efforts have been made to evaluate the potential applications of spent adsorbents in areas such as catalysis and energy storage devices.[28,29] Energy storage devices are essential components of modern energy systems. It enables efficient storage and delivery of electrical energy to meet intermittent supply.[30] Among the various technologies available, supercapacitors (also known as electrochemical capacitors) have emerged as promising candidates owing to their high power density, rapid charge–discharge capability, and excellent cycling stability.[30,31] These features make them promising candidates for high-performance applications, including hybrid electric vehicles, renewable energy systems, and portable electronic equipment, where rapid energy response and stability are required.[32] Their energy storage mechanism is based on the accumulation of electrostatic charge or fast, reversible redox reactions at the electrode–electrolyte interface. The device efficiency depends greatly on the physical and chemical properties of the electrode materials as well as the electrochemical stability of the electrolyte.[33,34] The potential of S-doped graphitic CN/ZIF composite adsorbent used for the adsorption of Pb^{2+} was used for the fabrication of a hybrid supercapacitor.[35] Similarly, activated carbon prepared from paper sludge was reportedly used for the adsorption of methylene blue dye, and the spent adsorbent was subsequently used as electrode material for a supercapacitor.[36]

This study valorises wastewater sludge to produce activated carbon for the efficient removal of MnO$_4^-$ from water, while the spent adsorbent is reused as an electrode material for energy storage, addressing secondary pollution. We hypothesise that the sludge-derived carbon (H-WSAC) can achieve over 90% MnO$_4^-$ removal within 10 min under optimal conditions, providing a clear focus for the experimental design and expected outcomes.

2 Materials and materials

2.1 Materials

Wastewater sludge (WS) was used as the precursor for the preparation of activated carbon. The sludge was collected from wastewater treatment plants (WWTPs) in South Africa as a waste

material. All other chemicals used in this research were purchased from Sigma-Aldrich. These chemicals include, but are not limited to, potassium permanganate (KMnO$_4$), sulphuric acid (H$_2$SO$_4$), hydrochloric acid (HCl), orthophosphoric acid (H$_3$PO$_4$), ethanol (C$_2$H$_5$OH), acetone (C$_3$H$_6$O), carbon black, polyvinylidene fluoride [PVDF, P-(C$_2$H$_2$F$_2$)$_n$–], and N-methyl-2-pyrrolidone (NMP, C$_5$H$_9$NO).

2.2 Methods

2.2.1 Preparation of activated carbon. 20 g of dried wastewater sludge (WS) was carbonised at 600 °C in a Lenton muffle furnace for 4 h to obtain wastewater sludge char (WSC). The WSC was soaked in a 30% (v/v) H$_3$PO$_4$ activating agent at a 1 : 10 ratio for 24 h. It was then washed to neutral pH and dried. The resulting activated carbon was weighed, rewashed, dried at 105 °C, pulverised, and sieved. The final powder-activated carbon, labelled H-WSAC, was stored for further characterisation and applications.

2.2.2 Adoption experiment. Adsorption processes were carried out using a batch adsorption experiment. The stock adsorbate solution (100 mg L^{-1} MnO$_4^-$) was prepared by dissolving the required amount of KMnO$_4$ in deionised water. Other working concentrations were prepared using serial dilution. In a typical run, 0.02 g of H-WSAC was contacted with a known concentration of MnO$_4^-$. The mixture was agitated on a thermostatic mechanical shaker for 180 min. After agitation, the mixture was filtered. The filtrate was analysed for residual MnO$_4^-$ using a spectrophotometer at a predetermined λ_{max} of 525 nm. The spent adsorbent, labelled Mn-WSAC, was dried and stored for supercapacitor applications. The effects of initial MnO$_4^-$ concentrations (5–100 mg L^{-1}), pH (2–10), contact time (5–180 min), and dosage (0.01–0.10 g) were investigated. The quantity adsorbed (q_e) and removal efficiency (R_{eff}) were calculated using eqn (1a) and (1b).

$$q_e = \frac{C_i - C_f}{m} \times V \tag{1a}$$

$$R_{eff} = \frac{C_i - C_f}{C_i} \times 100 \tag{1b}$$

where C_i and C_f are the initial and final concentrations (mg L^{-1}) of the adsorbate (MnO$_4^-$), respectively, m is the mass (g) of the adsorbent (H-WSAC), V is the volume (L) of the adsorbate used during the reaction, q_e is the quantity adsorbed (mg g^{-1}), and R_{eff} is the removal efficiency (%).

2.2.3 Fabrication of the electrode. The spent activated carbon (Mn-WSAC) was revalorised as the electrode material, and stainless steel (SS) was used as the current collector on which the electrode material was coated. Firstly, the surface of the stainless steel was washed thoroughly for 30 min through sonication in 3 M HCl, followed by acetone and ethanol. It was then rinsed with deionised water and finally dried. Then, a slurry of Mn-WSAC was made with carbon black and PVDF in an 8 : 1 : 1 ratio in the presence of NMP. The slurry was coated onto a 1 cm^2 area of the SS and then oven-dried at 80 °C for 8 h.

2.2.4 Characterisation. The properties of the H-WSAC as pristine activated carbon and the spent adsorbent (Mn-WSAC)

were investigated. Raman spectroscopy (WiTec confocal Raman microscope) was used to analyse the structural characteristics and to distinguish between crystalline and amorphous phases. Fourier-transform infrared spectroscopy (FTIR; PerkinElmer Spotlight 400) was employed to identify the surface functional groups. The crystal structure was determined using X-ray Diffraction (XRD; Rigaku diffractometer, Cu Kα radiation, $\lambda = 0.154$ nm) in a 2θ range of 10° to 80°. Scanning Electron Microscopy coupled with Energy Dispersive X-ray (SEM-EDX; JSM IT-300 microscope) was used for surface morphology and elemental compositions. The internal structural morphology and crystallinity were investigated using Transmission Electron Microscopy (TEM; JEOL JEM-2100F, operating at 200 kV). The surface charge of the H-WSAC was determined using the drift method.[37]

2.2.5 Determination of electrochemical properties. The electrochemical properties of the Mn-WSAC-based electrode were evaluated in a 1 M H_2SO_4 electrolyte using a BioLogic SP-300 potentiostat. Cyclic voltammetry (CV), galvanostatic charge–discharge (GCD), and electrochemical impedance spectroscopy (EIS) measurements were conducted using both three-electrode and two-electrode configurations. The specific capacitance (C_{sp}) was calculated from CV and GCD data using eqn (2a)–(2c), while the energy density (E_d) and power density (P_d) were determined using eqn (3a) and (3b), respectively:

$$C_{sp,CV} = \frac{A}{2kmV} \quad (2a)$$

$$C_{sp,GCD} = \frac{I \times \Delta t}{m \times \Delta V} \quad (2b)$$

$$C_{sp,GCD,2\text{-electrode}} = 4C_{sp,GCD} \quad (2c)$$

$$E_d = \frac{C_{csp} \times \Delta V^2}{2 \times 3.6} \quad (3a)$$

$$P_d = \frac{3600 \times E_d}{\Delta t} \quad (3b)$$

where $C_{sp,CV}$ and $C_{sp,GCD}$ denote specific capacitance (F g^{-1}) from cyclic voltammetry and galvanostatic-charge–discharged, respectively. A is the area of the shape under the curve (mA V), k is the scan rate (mV s^{-1}), m is the mass (g) of the electrode material, I is the current (mA), ΔV is the potential window range (V), Δt is the difference between charge and discharge time (s), E_d is the energy density (Wh kg^{-1}) and P_d is the power density (W kg^{-1}).

3 Results and discussion

3.1 Adsorption experiment

3.1.1 Effect of adsorption parameters. The information obtained from the adsorption of MnO_4^- is shown in Fig. 1, illustrating the effect of different adsorption parameters on the process. Fig. 1a demonstrates the effect of the initial MnO_4^- concentration on the adsorption capacity of H-WSAC at a 180 min contact time, an inherent pH of 6.8, a 0.02 g adsorbent dosage, and room temperature (25 °C). It is observed that

the adsorption capacity (q_e) of H-WSAC for MnO_4^- increases with increasing concentration. Specifically, the capacity increases from 5.65 mg g^{-1} at 5 mg L^{-1} to 78.36 mg g^{-1} at 100 mg L^{-1}. This increase is due to the higher affinity for the permanganate ion as its concentration increases, given a constant amount of H-WSAC and other parameters. The adsorption capacity of adsorbents generally increases with the increase in the concentration of the adsorbate because there is a greater driving force for molecules to bind to the surface of the adsorbent.[38] However, the removal efficiency increased only up to 98.4% of the 30 mg L^{-1} initial concentration of MnO_4^-, after which a reduction in efficiency set in. The decline in removal efficiency beyond this concentration indicates the saturation point, after which the binding sites have no more affinity for the adsorbate molecules.

Fig. 1b depicts the effect of contact between H-WSAC and the solution of MnO_4^- at a constant concentration of 100 mg L^{-1}, pH of 6.8, a 0.02 g adsorbent dosage, and room temperature (25 °C). The progress in the adsorption process is divided into three stages, namely the first stage (0–30 min), the second stage (30–90 min), and the third stage (90–180 min). The first stage, at 30 min, witnessed a swift reaction in which 38.88 mg g^{-1}, representing 31.10% of the initial concentration, was removed. The second proceeded slowly with 67.43 mg g^{-1} (53.94%), indicating an increase of 15.06 mg g^{-1} (22.84%) within 60 min from the first stage. At the third stage, the adsorption of MnO_4^- onto H-WSAC resulted in a slight increase of 18.81 mg g^{-1} (15.05%) within a 90 minutes interval from the second stage. The rapid reaction, the significant amount, and the high removal efficiency observed at the first stage resulted from the availability of adsorption sites during the early period of the adsorption process.[39]

The importance of pH in the adsorption process extends beyond determining the optimum condition of the parameter; it also affects the surface charge of adsorbents, the surface functional groups, and the degree of ionisation of the adsorbate molecules.[40] Fig. 1c represents the observation when the pH of the MnO_4^- solution was varied between pH 2 and 10, while a concentration of 100 mg L^{-1}, a 180 min contact time, a 0.02 g adsorbent dosage, and room temperature (25 °C) were maintained. The adsorption capacity (q_e) and the removal efficiency (R_{eff}) decline from 125.0 mg g^{-1} (100%) at pH 2 to 97.42 mg g^{-1} (77.93%) at pH 10. The result revealed that H-WSAC performed better in an acidic medium than in an alkaline medium. The significant amount of MnO_4^- adsorbed throughout the pH range is attributed to the pK_a value of $KMnO_4$, which is 2.17. It has been established that the molecules of adsorbates exist in ionic form at a pH greater than pK_a.[1,41] pH also provides insight into the mechanism of the process[13] based on the pHpzc result. The pHpzc of H-WSAC was determined to be 4.0 (Fig. SI-1). This result implies that below a pH of 4, the surface of H-WSAC is positively charged, and that is why the adsorption of negatively charged MnO_4^- is much favoured between pH 2 and 4. Additionally, the surface becomes negatively charged at a pH above the pHpzc, resulting in a reduction in adsorption capacity due to charge repulsion. Consequently, the mechanism of the adsorption of MnO_4^- onto H-WSAC is electrostatic attraction.[1]
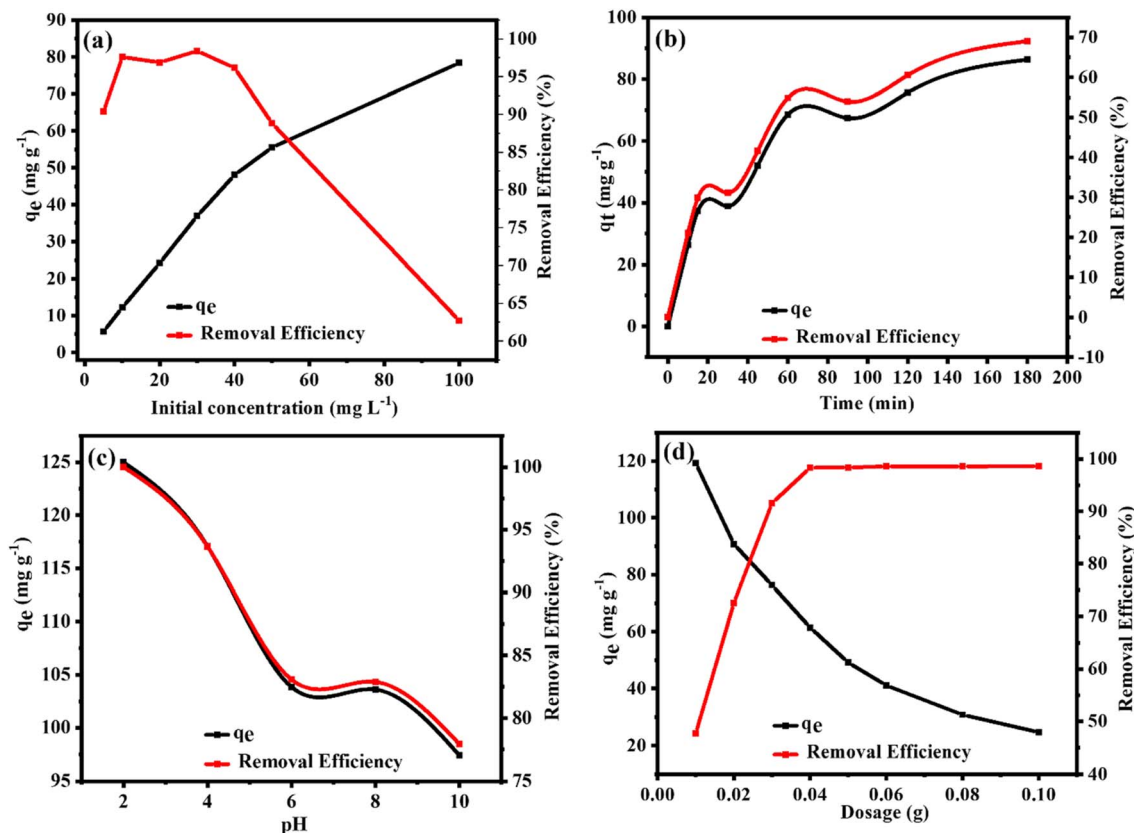
Fig. 1 Effect of (a) initial concentration (b) contact time (c) pH, and (d) adsorbent dosage on the adsorption of MnO_4^- onto H-WSAC.

Fig. 1d depicts the effect of the adsorbent dosage on the removal of MnO_4^- from aqueous solution. At a constant concentration of 100 mg L^{-1}, a 180 min contact time, inherent pH 6.8, and room temperature (25 °C), the adsorbent dosage was varied between 0.01 g and 0.10 g. It is observed that the q_e adsorbed decreases with an increase in adsorbent dosage from 119.2 mg g^{-1} at 0.01 g to 24.7 2 mg g^{-1} at 0.1 g. This observation is a consequence of the increased adsorbent dosage. In contrast, the amount of MnO_4^- at a particular concentration is fixed, and the adsorption capacity is defined per unit mass of the adsorbent (eqn (1a)).[42] The trend can also be attributed to the saturation of the adsorption sites at lower adsorbent dosages.[38] However, the removal efficiency increases with increasing dosage. The converse trend is due to the availability of more adsorption sites at higher dosages. At the same time, the initial concentration, which is a function of the removal efficiency, remains fixed (eqn (1b)). A similar trend was reported during the adsorption of organic and inorganic pollutants onto activated carbon. A comparison of the adsorption capacities of different adsorbents for MnO_4^- and the corresponding adsorption conditions is presented in Table 1.[43]

3.1.2 Adsorption isotherms. The adsorption data obtained from the effect of initial concentration were subjected to the Langmuir and the Freundlich isotherms to understand the relationship between the adsorbate and the adsorbent at a constant temperature. The fitness and suitability of the

isotherm model were based on the R^2 values. The plot of $\frac{C_e}{q_e}$ *vs.* C_e for the Langmuir isotherm (eqn (4a)), a R^2 value of 0.974 was obtained. In the case of Freundlich, the plot of log q_e *vs.* log C_e (eqn (5)) yielded a lower R^2 of 0.561. The graphs of the plots are shown in the SI (Fig. SI-2), and the obtained parameters are presented in Table 2.

$$\frac{C_e}{q_e} = \frac{1}{q_m K_L} + \frac{C_e}{q_m} \tag{4a}$$

$$R_L = \frac{1}{1 + K_L C_i} \tag{4b}$$

$$\log q_e = \log K_f + \frac{1}{n} \log C_e \tag{5}$$

where C_i and C_e are the initial and equilibrium concentrations of adsorbate respectively (mg L^{-1}), q_e is the amount of adsorbate adsorbed per unit mass of adsorbent (mg g^{-1}), q_m is the monolayer adsorption capacity (mg g^{-1}), K_L is the Langmuir adsorption constant (L mg^{-1}), R_L is the separation factor, n is the empirical parameter related to adsorption intensity, and K_f (mg g^{-1}) is the Freundlich constant representing the adsorption capacity.

The equilibrium adsorption data of MnO_4^- onto the H-WSAC indicate a monolayer adsorption and a homogeneous surface, in accordance with the Langmuir assumptions. The

Table 1 Comparison of adsorption capacities of different adsorbents for MnO_4^-

Adsorbent	Adsorption condition	Adsorption capacity (mg g^{-1})	Ref.
Pinecone biosorbent	2 mg L^{-1} initial conc., 24 h contact time, and 0.2 g adsorbent dosage	4.51	10
Coconut shell activated carbon	25 g adsorbent dosage, 60 min contact time, and 20 °C reaction temperature	23.94	12
Palm nutshell activated carbon	50 mg L^{-1} initial conc., pH 6.5, and 25 °C reaction temperature	8.4	13
Neem leaves powder	100 mg L^{-1} initial conc., 6 h contact time, 0.02 g adsorbent dosage, and 30 °C reaction temperature	45.31	44
Oxalic acid modified biosorbent	100 mg L^{-1} initial conc., 5 h 20 min contact time, 0.02 g adsorbent dosage, and 27 °C reaction temperature	79.89	45
Wastewater sludge activated carbon (H-WSAC)	100 mg L^{-1} initial conc., 180 min contact time, an inherent pH of 6.8, a 0.02 g adsorbent dosage, and 25 °C reaction temperature	78.36	This work

Table 2 Adsorption isotherm parameters

Isotherm	Langmuir parameters			Freundlich parameters		
	R^2	q_m (mg g^{-1})	R_L	R^2	K_f (mg g^{-1})	n
H-WSAC	0.974	83.3	0.022–0.32	0.473	1.14	2.54

isotherm model assumes that the adsorption sites are homogeneous with equal energy, and the adsorbate molecules bind on these sites in a single layer.[46] The monolayer adsorption capacity (q_m) is 83.3 mg g^{-1}, which is in close agreement with the experimental value of 78.3 mg g^{-1} at 100 mg L^{-1}. Further evaluation of the R_L, a critical parameter of the Langmuir isotherm, known as the separation factor, indicates that the adsorption of MnO_4^- onto H-WSAC is favourable over a range of concentration investigated. R_L value between 0 and 1 is favourable; it is unfavourable when greater than 1, and regarded as linear when it is equal to 1.[47] The fact that the Freundlich isotherm, which describes a heterogeneous surface, did not fit the adsorption data confirms the homogenous surface suggested by the Langmuir isotherm. Consequently, its parameters (Table 2) are not considered.

3.1.3 Adsorption kinetics. Adsorption kinetics help to better understand how time affects the reaction by examining the rate, and offer insights into the mechanism behind the adsorption process.[48] Here, the kinetics of the adsorption of MnO_4^- onto H-WSAC were elucidated using pseudo-first-order (PFO) and pseudo-second-order (PSO) with eqn (6) and (7), respectively.

$$\ln(q_e - q_t) = \ln q_e - k_1 t \qquad (6)$$

$$\frac{t}{q_t} = \frac{1}{k_2 q_e^2} + \frac{1}{q_e} t \qquad (7)$$

where q_e and q_t are the quantities of MnO_4^- adsorbed at equilibrium and at time t, respectively, (mg g^{-1}); k_1 is the pseudo-first-order rate constant (min^{-1}) and k_2 is the pseudo-second-order rate constant (g mg^{-1} min^{-1}).

The data obtained from the effect of time treated with each of the equations. The conditions for the equations to perfectly describe the adsorption process are a good R^2 and closeness of the calculated quantity adsorbed ($q_{e,cal.}$) with that of the experimental ($q_{e,exp.}$). The plots of the two kinetic models are presented in the SI (Fig. SI-3), and the obtained parameters are presented in Table 3. It is observed that both the PFO and PSO fit the adsorption data with R^2 values of 0.7528 and 0.9754, respectively. The PFO gave a moderate fitness, but there is a significant discrepancy between the $q_{e,cal.}$, and $q_{e,exp.}$. Therefore, the result can't be relied on to conclude on the likely mechanism. The PSO not only yielded a better R^2 value but also gave a $q_{e,cal.}$ that is closer to the experimental one. Consequently, it can be suggested that the mechanism is chemisorption.

3.2 Physicochemical and structural characterisation

The physicochemical properties of the adsorbent (H-WSAC) and the spent adsorbent (Mn-WSAC) are outlined in this section. Fig. 2a displays the FTIR spectra, which reveal the functional groups on the surfaces of H-WSAC and Mn-WSAC. It is clear that there is no significant difference in the spectra before and after the adsorption of MnO_4^-. However, it is observed that their surfaces are characterised by –OH stretching vibrations at approximately 3426 cm^{-1}. The peak at approximately 1595 cm^{-1} is attributed to –C=C of aromatic rings.[49] The prominent peak at 1043 cm^{-1} is due to the PO_4^{3-} introduced by the activating agents.[50] Other peaks at ~797, ~ 664, and ~455 cm^{-1} are attributed to Si–H, Si–O–C, and Si–O–Si.[51,52] The H-WSAC and Mn-WSAC obtained after MnO_4^- adsorption were further characterised by Raman spectroscopy (Fig. 2b). This technique

Table 3 Adsorption kinetic parameters

Kinetic model	$q_{e,exp.}$ (mg g^{-1})	Pseudo-first order			Pseudo-second order		
		R^2	k_1 (min^{-1})	$q_{e,cal.}$ (mg g^{-1})	R^2	k_2 (g mg^{-1} min^{-1})	$q_{e,cal.}$ (mg g^{-1})
H-WSAC	86.3	0.7528	1.04	821.6	0.9754	0.0003	100

is essential for carbon materials.[53] Both spectra show two notable peaks at 1366 cm^{-1} (D-band) and 1598 cm^{-1} (G-band), along with a broad peak between 2500 and 3000 cm^{-1} (2D-band). The D-band indicates the double resonance of disordered carbon. The intensity of the D-band reflects the degree of disorder in the carbon structure.[54] Meanwhile, the G-band indicates the presence of C=C vibrations of graphite (sp^2 hybridisation).[55] The degree of graphitisation or disorderliness (R_I) was calculated using the ratio of the intensities of the D and G bands, as shown in eqn (8).

$$R_I = \frac{I_D}{I_G} \quad (8)$$

where R_I is the degree of graphitisation or disorderliness in the carbon structure, I_D and I_G are the intensities of the D-band and the G-band, respectively. The values of R_I observed for the H-WSAC before and after the adsorption process are 0.80 and 0.79, respectively. The low value of R_I indicates the presence of a less disordered graphitised carbon structure.[56] It is also observed that there is no difference between R_I value of H-WSAC before and after the adsorption of MnO_4^-. This suggests that MnO_4^- has no impact on the degree of graphitisation. However, the appearance of a peak at ~472 cm^{-1} after the adsorption is a confirmation of the introduction of a foreign substance onto the surface of the H-WSAC. This band is attributed to the presence of MnO_2, especially those with layers such as birnessite and spinel.[57,58] This shift is likely caused by the environment in which the MnO_2 finds itself. Furthermore, the peak at 2799 cm^{-1} is associated with 2D as a result of the overtone of carbon, indicating the presence of a layered structure.[53]

Fig. 3a and b show the surface morphology of H-WSAC before and after MnO_4^- adsorption, as revealed by scanning electron microscopy (SEM). The SEM images display flaky particles with irregular pores. These pores are formed due to the action of H_3PO_4 used as the activating agent. There are no significant differences in the overall morphology of both images. This is because the initial H-WSAC already contains some metals from its precursors, wastewater sludge. Similarly, the TEM images in Fig. 3c and d illustrate a hierarchical, disordered carbon structure with pores. The heterogeneity of the H-WSAC activated carbon is also evident in the TEM images, highlighted by black spots (yellow circles) before and after adsorption. EDX spectra (Fig. 3e and f) confirm the presence of different elemental compositions in the activated carbon. Notably, a significant percentage of Mn appears in the EDX spectrum after adsorption. The result confirms that MnO_4^- adsorption occurred on the surface of H-WSAC, leading to removal.

Fig. 4 presents the XRD patterns of H-WSAC and Mn-WSAC together with the reference cards from the American Mineralogist Crystal Structure Database (AMCSD) used for phase identification and indexing. The following cards were used: carbon (amcsd 0013020; space group: P6/mmm), quartz (amcsd 0011007; space group: P3$_1$21), calcite (amcsd 0000098; space group: R$\bar{3}$c), and carbonate-hydroxylapatite (amcsd 0003642; space group: P6$_3$/m). The diffraction patterns of both H-WSAC and Mn-WSAC obtained after the adsorption of MnO_4^- are similar, suggesting no change to the structure of activated carbon. The prominent peaks at $2\theta = 20.7°$ and $26.5°$ correspond to the characteristic peaks of carbon and quartz (SiO_2),
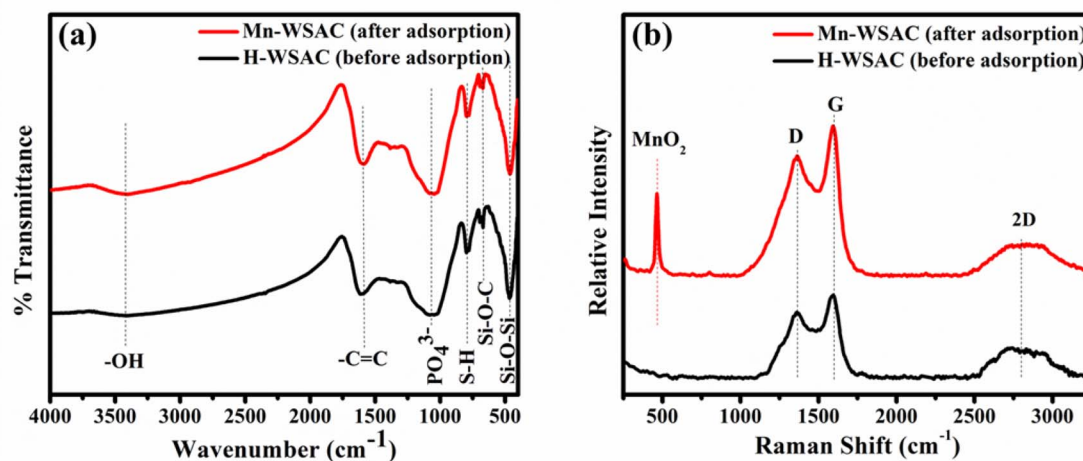

Fig. 2 (a) FTIR spectra and (b) Raman spectra of H-WSAC (before adsorption) and Mn-WSAC (after adsorption) of MnO_4^-.
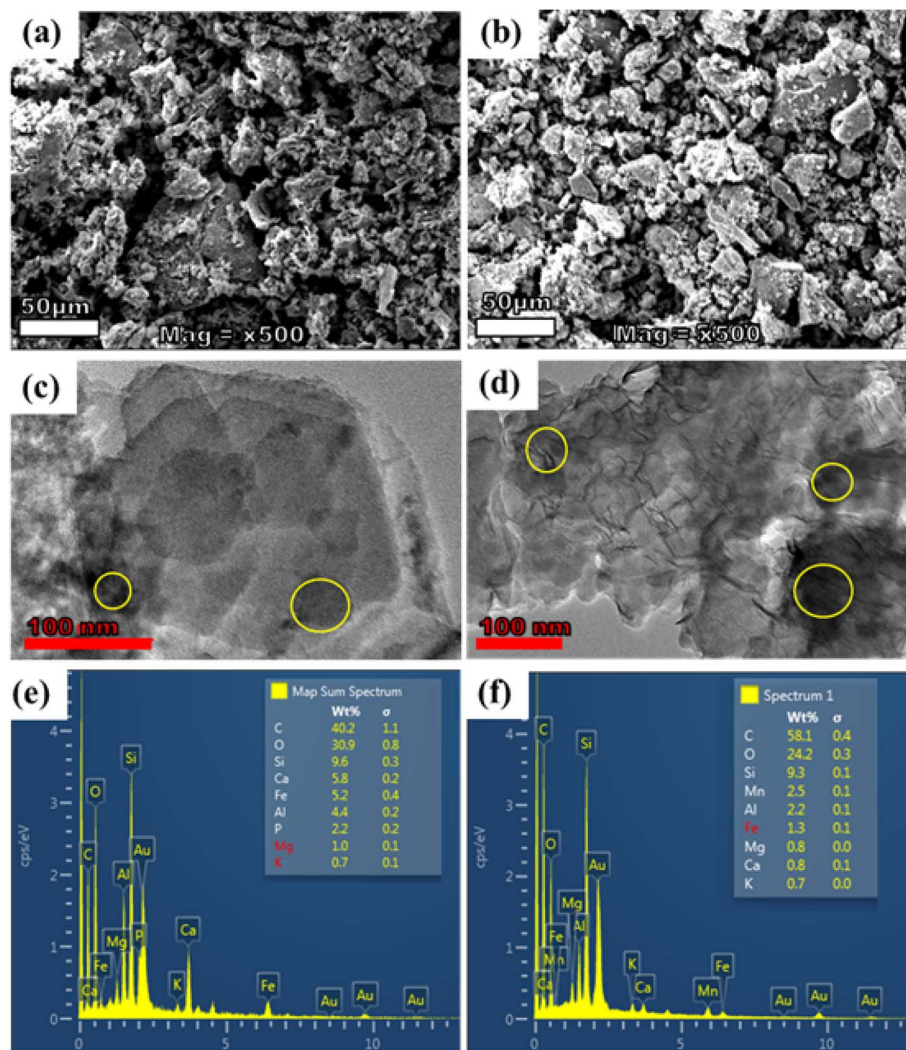
Fig. 3 (a and b) SEM images, (c and d) TEM images, and (e and f) EDX spectra of H-WSAC (before adsorption) and Mn-WSAC (after adsorption) of MnO_4^- respectively.

respectively. The peak at 29.7° is a characteristic peak of calcite ($CaCO_3$), but it is very weak. Other forms of calcite in the H-WSAC adsorbent may have been converted to hydroxylapatite during the activation process with H_3PO_4 acid.

3.3 Electrochemical properties

3.3.1 Three-electrode system. The electrochemical behaviour of the spent adsorbent (Mn-WSAC) in a three-electrode system with 1 M H_2SO_4 is presented in Fig. 5a–d. Cyclic voltammetry (CV) was measured over a potential range of 0 to 1.0 V at various scan rates. The CV investigation revealed a pseudo-behavioural supercapacitor (Fig. 5a), characterised by a distorted rectangular shape of electric double-layer capacitance (EDLC) behaviour. The curve is a characteristic of a combined EDLC and pseudocapacitive.[59] This suggests a synergistic property of non-faradaic and faradaic charge storage mechanisms. Therefore, there is a need to determine the percentage contribution of the process.

Furthermore, the quasi-symmetry between the anodic and cathodic peaks suggests a good reversibility of the reduction at the electrode–electrolyte interface. However, the slight deviation from perfect symmetry can be attributed to limitations during ion transport due to internal resistance. Even at a relatively high scan rate (100 mV s^{-1}), the material retains its electrochemical characteristics, indicating excellent ionic/electronic conductivity, as well as rapid charge transport.[60]

Considering the combined capacitive and pseudo-capacitive storage mechanisms observed in the CV curve, a plot of eqn (9b) of Dunn's method was applied. The CV data obtained at a scan rate range of 2 to 100 mV s^{-1} were treated by eqn (10a) and (10b) to provide insight into the percentage contribution of each mechanism.

$$i = av^b \tag{9a}$$

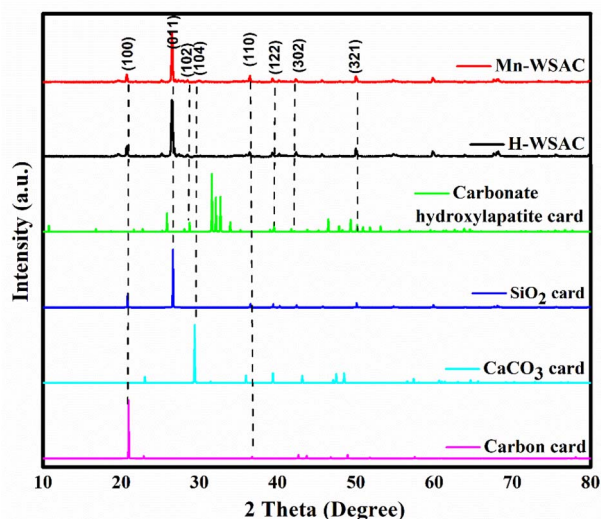$$\log i = \log a + b \log v \tag{9b}$$

Fig. 4 XRD pattern of H-WSAC (before adsorption) and Mn-WSAC (after adsorption) of MnO_4^-.

$$i_{(V)} = k_1 \nu + k_2 \nu^{0.5} \quad (10a)$$

$$\frac{i_{(V)}}{\nu^{0.5}} = k_1 \nu^{0.5} + k_2 \quad (10b)$$

where i is the current at a fixed potential (A), ν is the scan rate (mV s^{-1}), a is an adjustable parameter, and b is a variable that depends on whether the contribution comes from capacitive or diffusion processes. The value of $b = 0.5$ indicates diffusion dominance, while $b = 1$ indicates surface capacitive effects. A value between 0.5 and 1 suggests a combined mechanism. k_1 and k_2 are slope and intercept, respectively, that can be obtained from a plot of eqn (10b). Substituting the values into eqn (10a) yields the magnitude of capacitive and pseudocapacitive behaviours, which can be expressed as a percentage.[61,62]

Fig. 5b and c present the results of Dunn's plot and the representation of each storage mechanism. The value of b is 0.62, indicating a more diffusion-controlled mechanism and further suggesting pseudocapacitive behaviour than EDLC, which is fundamental to supercapacitors. The percentage contributions of each mechanism are depicted in Fig. 5c, as obtained from the application of eqn (10b) (plot in Fig. SI-4), confirming the information provided by the value of b obtained from the Dunn plot. This scenario of a higher diffusion-controlled (pseudocapacitive) mechanism is likely due to the combined effect of the adsorbed MnO_4^- and the other metals present in the pristine activated carbon, as revealed by the EDX analysis (Fig. 3e and f). Furthermore, the redox properties of MnO_4^- tend to enhance the pseudocapacitance. The redox reaction of MnO_4^- in an acidic medium, such as 1 M H_2SO_4 used as electrolyte, is given in eqn (11). It was posited that the introduction of redox-active ions into the electrolyte increases the pseudocapacitance.[63,64] However, the surface contribution (capacitive) increases with an increase in scan rate since ions from the electrolytes do not have enough time to travel into the inner parts of the electrode at higher scan rates.[65]
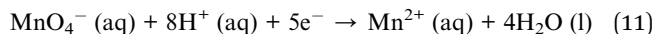
$$MnO_4^- \text{ (aq)} + 8H^+ \text{ (aq)} + 5e^- \rightarrow Mn^{2+} \text{ (aq)} + 4H_2O \text{ (l)} \quad (11)$$

Fig. 5d presents the results of galvanostatic charge–discharge (GCD) analyses of the spent adsorbent at various current densities (0.1 to 0.5 A g^{-1}). The curves display a typical triangular-like pattern of capacitive behaviour, but with a slight deviation. This deviation can be attributed to the pseudocapacitive behaviour of the material. This observation aligns with the results seen in the CV. As the current density increases, the specific discharge decreases, leading to a reduction in specific capacitance. The longest discharge time and highest specific capacitance are observed at lower current densities because there is more time for electrolyte ions to move through the electrode material. As a result, charge storage is more complete and efficient, resulting in higher capacitance. The charge and discharge occurred too quickly for the completion of ion diffusion at higher scan rates, resulting in less interaction of ions at the electrode surface, which in turn leads to a lower specific capacitance.[66] The specific capacitances at 0.1, 0.5, and 1.0 A g^{-1} are 517.9, 143.5, and 92.0 F g^{-1}, respectively. Fig. 5e presents the comparative specific capacitance (C_{sp}) (F g^{-1}) from the GCD and CV (inset) curves. It is observed that the capacitance decreases with an increase in the current density and scan rate.

Fig. 5f presents the Nyquist plot of the electrochemical impedance spectroscopy (EIS) of the Mn-WSAC in 1 M H_2SO_4 measured between 0.01 and 100 kHz. EIS is a crucial method for investigating electrochemical kinetics and mass transport processes at the electrode/electrolyte interface. The plots display the physical components that give insight into the resistance and capacitance of the system. These include the point at which the plot intercepts the real axis at high frequency, which corresponds to the solution resistance (R_s). Following this is a depressed semicircle at mid-frequency. The diameter of this semicircle represents the charge transfer resistance (R_{ct}). The third component is the slope at a lower frequency, which is referred to as the Warburg tail. Equivalent circuit fitting of the experimental data was carried out to deconvolute and quantify the identified physical components. From the equivalent circuit fitting, R_s and R_{ct} are 0.097 Ω and 110.7 Ω, respectively. The value of R_{ct}, which is inversely proportional to the rate of the electrochemical reaction,[67] is not too bad for efficient charge transfer at the electrode/electrolyte interface. The presence of a constant phase element (CPE) is attributed to non-ideal capacitive behaviour observed in the process.[68,69] Similarly, the presence of Warburg diffusion indicates that mass transport plays a crucial role in the overall cell impedance. The slope of the Warburg tail slightly deviated from a perfect diffusion (45°), suggesting a capacitive effect.[70,71]

3.3.2 Two-electrode system. The electrochemical performance of the spent adsorbent (Mn-WSAC) was further investigated in a two-electrode setup. The Mn-WSAC was used to prepare the two identical electrodes used in the setup. This created a symmetrical two-electrode setup with 1 M H_2SO_4 as the electrolyte. Fig. 6a shows the CV results of the setup at various scan rates, ranging from 2 to 50 mV s^{-1}. It is observed that the area under the CV curves increases with an increase in
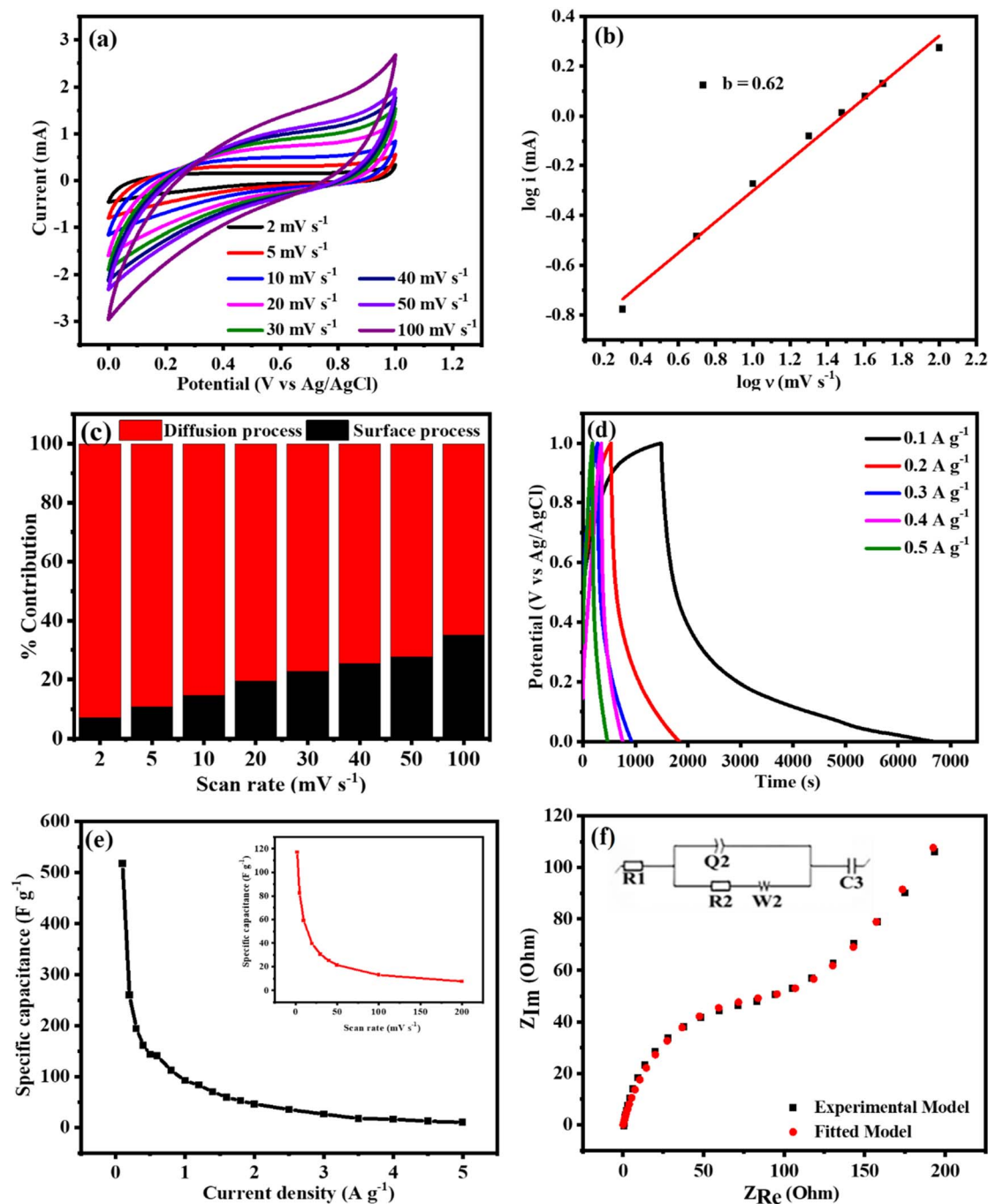
Fig. 5 (a) CV at different scan rates (b) log of current *vs.* log of scan rate (c) percentage contribution of storage mechanism at different scan rates (d) GCD at different current densities (e) specific capacitance *vs.* current density (inset: specific capacitance from CV) *vs.* scan rate, and (f) Nyquist plot (inset: fitted equivalent circuit) from EIS measurement for Mn-WSAC in 1 M H_2SO_4.

the scan rate at a stable geometry. The preservation of geometry at a relatively high scan rate of 50 mV s^{-1} demonstrates excellent and fast ion transport. The geometry of the CV curves exhibits a more rectangular shape for EDLC, with a display of redox peaks, compared to the three-electrode system. This agrees with the information revealed in the three-electrode system by the application of Dunn's method, that the charge

storage mechanism is a combination of capacitive and diffusion processes.

Having gathered information, such as the operating potential window from the CV curve at different scan rates, the ability to utilise the spent adsorbent in an energy storage device was supported by a galvanostatic charge–discharge study. Fig. 6b presents the GCD profiles at various current densities (0.5 to 5.0 A g^{-1}). The quasi-triangular shape obtained suggests the
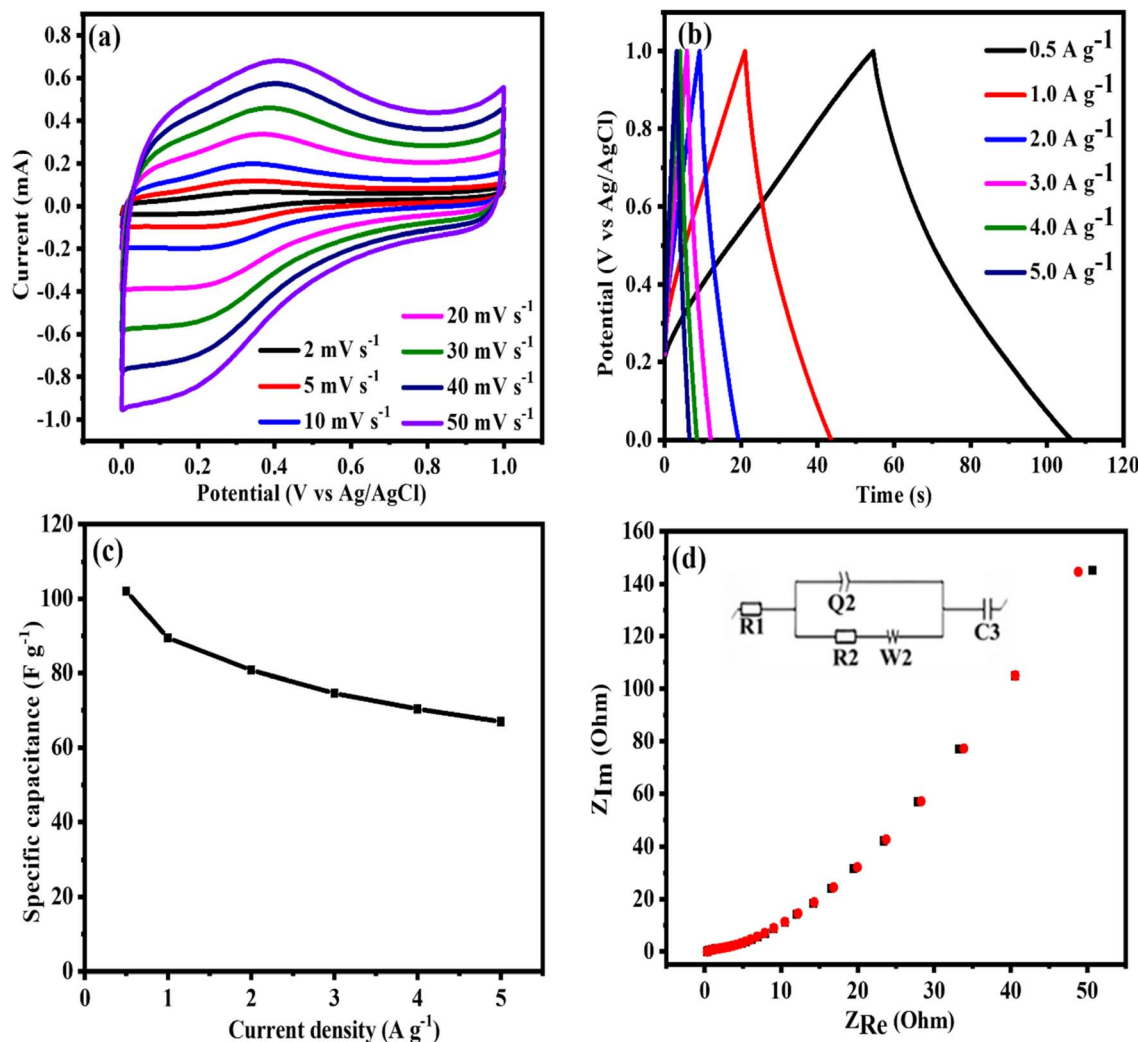
Fig. 6 (a) CV at different scan rates (b) GCD at different current densities (c) specific capacitance against current density, and (d) Nyquist plot (inset: fitted equivalent circuit) from EIS measurement for Mn-WSAC in 1 M H_2SO_4.

capacitive nature of the material, which contains activated carbon, and tends to exhibit more EDLC behaviour and charge transport properties of the electrolyte.[72–74] A slight deviation from a perfect triangle indicates the presence of a redox reaction, leading to a pseudoapacitance-like behaviour.[75] The specific capacitance (C_{sp}) in the device decreases with an increase in the current density (Fig. 6c). The values of C_{sp} at 0.5, 1.0, 2.0, 3.0, 4.0, and 5.0 A g^{-1} are 102.0, 89.5, 80.8, 74.6, 70.4, and 67.0 F g^{-1}, respectively. The significant value of C_{sp} at relatively high current density underscores the potential of the spent adsorbent (Mn-WSAC) as an electrode material for energy storage.

EIS study provides insight into the kinetics of charge transfers and describes the electrochemical reaction process. Fig. 6d shows the Nyquist plot obtained from the EIS measurement. The experimental data were fitted using Z-fit on BioLogic EC software with an appropriate circuit. The circuit is composed of R_s (solution resistance), R_{ct} (charge transfer resistance), and the Warburg diffusion element (W), with the CPE in parallel to the R_{ct}, similar to that of the three-electrode system. The values of R_s

and R_{ct} from the fitting are 0.26 and 3.45 Ω, respectively; these values are in good agreement with the experimental values of 0.32 and 3.48 Ω. Low R_s and R_{ct} values are suitable for favourable charge transport properties and improved device performance.[76,77]

The capacitance retention against the number of cycles, associated with the charge–discharge process (inset), is shown in Fig. 7a. Over 15 000 cycles, the Mn-WSAC device demonstrated an impressive ability to retain 83.15% of its specific capacitance. The stability over 15 000 cycles was monitored with EIS measurements at every 5000th cycle (Fig. 7b). It is physically evident that the slope of the Warburg tail deviates more from 45° as the number of cycles increases. The fitting of the experimental data into an appropriate circuit revealed that the R_{ct} values are 3.92 Ω, 3.97 Ω, and 5.54 Ω for the 1st, 2nd, and 3rd 5000 cycles, respectively. This observation probably results from electrolyte degradation or a change in electrode morphology.[78,79] This is also likely to account for the little reduction in capacitance that occurs after the 15 000th charge–discharge cycle. Furthermore, a Ragone curve was plotted (Fig. 7c) to illustrate
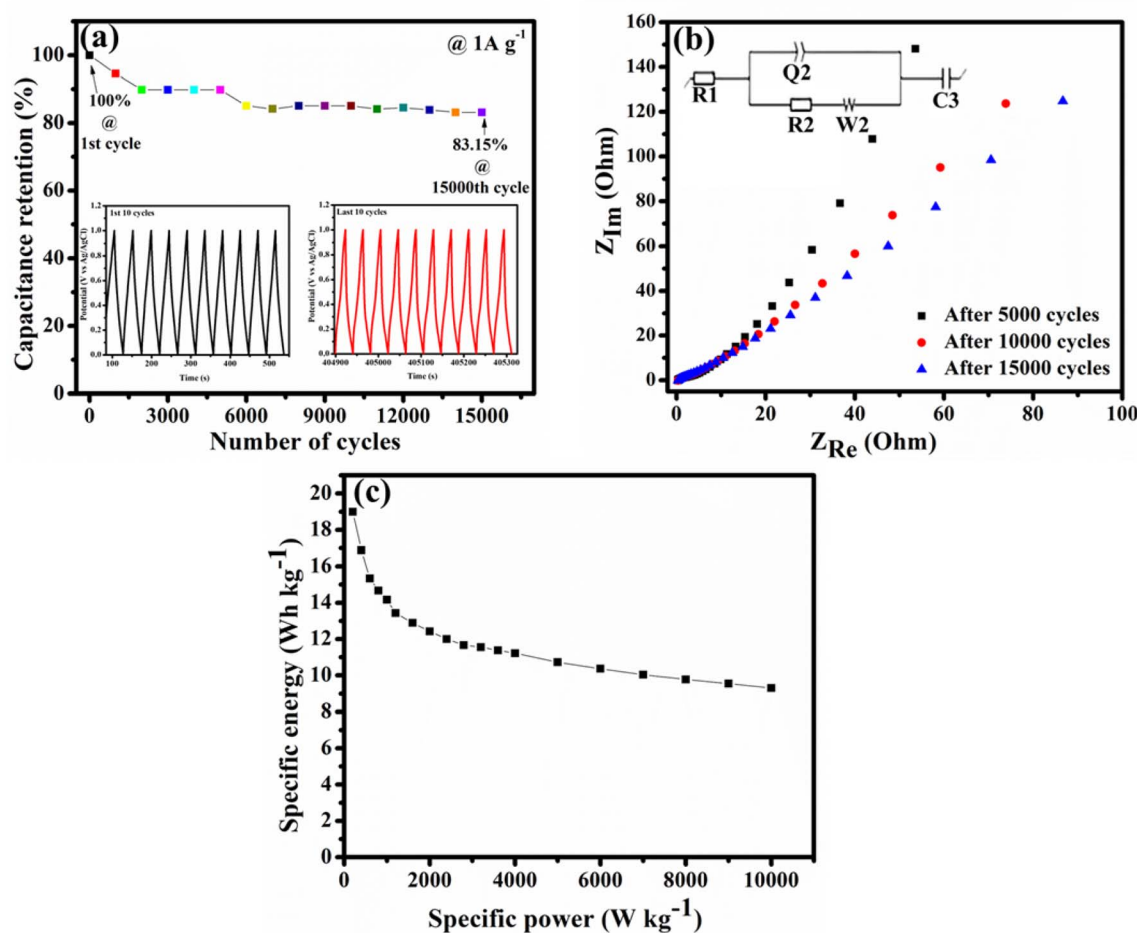
Fig. 7 (a) % Capacitance retention in 15 000 cycles (b) Nyquist plot (inset: fitted equivalent circuit) from EIS measurement after each 5000 cycles, and (c) Ragone plot of the device.

the relationship between specific energy and power at various current densities. The energy and the power densities of the Mn-WSAC device at a current density of 0.5 A g^{-1} are 14.16 Wh kg^{-1} and 1000 W kg^{-1}, respectively.

4 Conclusion

In conclusion, this study has demonstrated the potential of utilising wastewater sludge-derived activated carbon as an adsorbent for the adsorption of MnO$_4^-$ from water, as well as the application of the spent adsorbent in an energy storage device. The adsorption capacity of H-WSAC for MnO$_4^-$ is influenced by various adsorption parameters, including the initial concentration of MnO$_4^-$, contact time, pH, and dosage. An adsorption capacity of 78.36 mg g^{-1} (62.64%) at a concentration of 100 mg L^{-1} was achieved. The results of Raman spectroscopy and energy-dispersive X-ray spectroscopy (EDX) indicated changes in the properties of H-WSAC after the adsorption of MnO$_4^-$. The performance of the spent adsorbent (Mn-WSAC) as an electrode material in an energy device is noteworthy, with a significant specific capacitance (102 F g^{-1}), energy density (14.16 Wh kg^{-1}), and power density (1000 W

kg^{-1}) at a 0.5 A g^{-1} current density. The percentage retention at the end of 15 000 cycles, which is 83.15%, is another highlight of the study. Ultimately, it is posited that there is a possibility of valorising wastewater sludge into a water treatment adsorbent, and an excellent potential for revalorising the spent adsorbent in an energy storage device such as supercapacitors. Consequently, waste management of the sludge can be achieved through the valorisation process, and the secondary waste of the spent adsorbent can also be taken care of.

Author contributions

Moshawe J. Madito: conceptualisation, data curation, software, visualisation, validation, writing – review & editing, supervision. Thabo T. I. Nkambule: conceptualisation, supervision, project administration. Mojeed O. Bello: investigation, methodology, writing – original draft, formal analysis, data curation, visualisation.

Conflicts of interest

There is no conflict to declare.

Data availability

Data is available on request from the authors.

Supplementary information is available. See DOI: **https://doi.org/10.1039/d5ra06892d**.

Acknowledgements

References

1 H. A. Al-Aoh, *Mater. Res. Express*, 2019, **6**, 115102, DOI: **10.1088/2053-1591/ab4668**.

2 S. T. McBeath and N. J. D. Graham, *Sep. Purif. Technol.*, 2021, **260**, 118252, DOI: **10.1016/j.seppur.2020.118252**.

3 K. Piezer, L. Li, Y. Jeon, A. Kadudula and Y. Seo, *Process Saf. Environ. Prot.*, 2021, **148**, 400–414, DOI: **10.1016/j.psep.2020.09.058**.

4 B. R. Gutierrez-Aguirre, R. E. Llave-Davila, L. A. Olivera-Montenegro, E. Herrera-Nuñez and L. A. Marzano-Barreda, *Int. J. Food Sci.*, 2023, **2023**, 4650023.

5 B. P. Mabusela, Z. A. Belay, B. Godongwana, N. Pathak, P. V. Mahajan, P. M. K. Mathabe and O. J. Caleb, *S. Afr. J. Plant Soil*, 2021, 347–360, DOI: **10.1080/02571862.2021.1938260**.

6 C. M. Mfoumou, F. Ngoye, P. Tonda-Mikiela, M. L. Berthy, B. M. Spenseur and G. R. F. Tchouya, *Open J. Inorg. Chem.*, 2023, **13**, 25–42.

7 T. Umar, L. Wenjing, H. Feng, W. Feng, M. Bin, Z. Umar, M. Naeem, A. S. Umar, S. Asif, M. Usman and D. Ganzhen, *Pak. Vet. J.*, 2024, **44**, 214–221.

8 A. M. Badran, U. Utra, N. S. Yussof and M. J. K. Bashir, *Separations*, 2023, **10**, 565.

9 R. K. Verma, R. Kapoor, S. K. Gupta and R. R. Chaudhari, *Pharm. Chem. J.*, 2014, **1**, 20–25.

10 A. D. Nieva, B. T. Doma and H. P. Chao, *IOP Conf. Ser. Earth Environ. Sci.*, 2018, **191**, 012034, DOI: **10.1088/1755-1315/191/1/012034**.

11 A. Hassan, R. K. Pandey, A. Chakraborty, S. A. Wahed, T. R. Rao and N. Das, *Soft Matter*, 2024, **20**, 7832–7842.

12 F. Aprilliani, E. Warsiki and A. Iskandar, *IOP Conf. Ser. Earth Environ. Sci.*, 2018, **141**, 012003.

13 C. Mve Mfoumou, P. Tonda-Mikiela, F. Ngoye, M. Berthy Lionel, B. Mougnala Spenseur, A. Sachse, S. Mignard and G. Raymond Feuya Tchouya, *J. Environ. Pollut. Hum. Heal.*, 2022, **10**, 58–70.

14 A. Cano-Larrotta, R. Castellnou, E. J. Pastor, J. Subirats, V. Matamoros and E. Uggetti, *J. Environ. Manage.*, 2024, **370**, 122716.

15 V. Kumar, A. K. Chopra and A. Kumar, *Arch. Agric. Environ. Sci.*, 2017, **2**, 340–347.

16 J. Fernandes, P. J. Ramísio and H. Puga, *Eng*, 2024, **5**, 2633–2661.

17 B. Koul, D. Yadav, S. Singh, M. Kumar and M. Song, *Water*, 2022, **14**(21), 3542, DOI: **10.3390/w14213542**.

18 S. Kato and Y. Kansha, *Environ. Sci. Pollut. Res.*, 2024, **31**, 51064–51097.

19 H. Zhou, L. Wei, D. Wang and W. Zhang, *Environ. Int.*, 2022, **166**, 107378.

20 S. Mushtaq, F. Jamil, M. Hussain, A. Inayat, K. Majeed, P. Akhter, M. S. Khurram, A. Shanableh, Y. M. Kim and Y. K. Park, *Environ. Res.*, 2024, **249**, 118326.

21 K. H. Chua, W. L. Cheah, C. F. Tan and Y. P. Leong, *IOP Conf. Ser. Earth Environ. Sci.*, 2013, **16**, 012118.

22 H. Thakur, A. Dhar and S. Powar, *Results Eng.*, 2022, **16**, 100617.

23 D. Altheman, L. Andréia Gachet, M. Siviero Pires and R. C. C. Lintz, *Mater. Today Proc.*, 2023, 418.

24 X. Chen, S. Jeyaseelan and N. Graham, *Waste Manage.*, 2002, **22**, 755–760.

25 N. M. Y. Al-mahbashi, S. R. M. Kutty, A. H. Jagaba, A. Al-nini, A. T. Sholagberu, B. N. S. Aldhawi and U. Rathnayake, *Case Stud. Chem. Environ. Eng.*, 2023, **8**, 100437.

26 J. B. Rial and M. L. Ferreira, *Sci. Total Environ.*, 2022, **823**, 153370, DOI: **10.1016/j.scitotenv.2022.153370**.

27 B. G. Fouda-Mbanga, O. P. Onotu and Z. Tywabi-Ngeva, *Green Anal. Chem.*, 2024, **11**, 100156.

28 J. Ma and C. Liu, *J. Colloid Interface Sci.*, 2021, **582**, 1107–1115.

29 O. I. Adeiga and K. Pillay, *ACS Omega*, 2024, **9**, 38348–38358.

30 Z. Li and D. Deusen, *Int. J. Hydrogen Energy*, 2025, **102**, 1055–1074.

31 K. Dissanayake and D. Kularatna-Abeywardana, *J. Energy Storage*, 2024, **96**, 112563.

32 M. Salaheldeen, T. N. A. Eskander, M. Fathalla, V. Zhukova, J. M. Blanco, J. Gonzalez, A. Zhukov and A. M. Abu-Dief, *Batteries*, 2025, **11**, 232.

33 M. F. Iqbal, F. Nasir, F. Shabbir, Z. U. D. Babar, M. F. Saleem, K. Ullah, N. Sun and F. Ali, *Adv. Energy Sustain. Res.*, 2025, 2400412.

34 A. Patel, S. K. Patel, R. S. Singh and R. P. Patel, *Discov. Nano*, 2024, **19**, 188.

35 S. Acharya, S. De, A. Ganguly, B. K. Mishra and G. C. Nayak, *Environ. Sci. Nano*, 2024, **11**, 1654–1670.

36 A. Durairaj, T. Sakthivel, S. Ramanathan, A. Obadiah and S. Vasanthkumar, *Cellulose*, 2019, **26**, 3313–3324.

37 A. Bülbül, A. Delibaş and R. Coşkun, *Biomass Convers. Biorefinery*, 2025, **15**, 23227–23242.

38 A. Hashem, C. O. Aniagor, S. Farag, M. Fikry, A. A. Aly and A. Amr, *Waste Manag. Bull.*, 2024, **2**, 172–183.

39 F. Chen, M. Hong, W. You, C. Li and Y. Yu, *Appl. Surf. Sci.*, 2015, **357**, 856–865.

40 M. Fakioğlu and Y. Kalpaklı, *RSC Adv.*, 2022, **12**, 26504, DOI: **10.1039/d2ra04501j**.

41 M. A. Zazouli, A. Azari, S. Dehghan and R. S. Malekkolae, *Water Sci. Technol.*, 2016, **74**, 2021–2035.

42 A. A. G. Khamseh, S. A. Ghorbanian, Y. Amini and M. M. Shadman, *Sci. Rep.*, 2023, **13**, 1–12.

43 D. O. Ozcan, M. C. Hendekci and B. Ovez, *Heliyon*, 2024, **10**, e32792.

44 H. A. Al-Aoh, *Mater. Res. Express*, 2019, **6**, 115102.

45 S. A. Bani-Atta, *Sci. Rep.*, 2022, **12**, 4547.

46 S. Alfnan, A. Awotunde, G. Glatz, S. Adjei, I. Alrumaih and A. Gowida, *J. Petrol. Sci. Eng.*, 2021, **207**, 109172, DOI: **10.1016/j.petrol.2021.109172**.

47 N. Ayawei, A. N. Ebelegi and D. Wankasi, *J. Chem.*, 2017, 3039817, DOI: **10.1155/2017/3039817**.

48 M. G. dos Santos, L. D. Paquini, P. H. L. Quintela, L. P. R. Profeti and D. Guimaraes, *ACS Omega*, 2025, **10**, 20326–20340.

49 M. Jahan and F. Feni, *Adv. Mater. Phys. Chem.*, 2022, **12**, 106–123.

50 Z. Elouear, J. Bouzid, N. Boujelben, M. Feki, F. Jamoussi and A. Montiel, *J. Hazard. Mater.*, 2008, **156**, 412–420.

51 N. A. M. Barakat, O. M. Irfan and H. M. Moustafa, *Molecules*, 2023, **28**, 296.

52 D. M. Widjonarko, J. Jumina, I. Kartini and N. Nuryono, *Indones. J. Chem.*, 2014, **14**, 143–151.

53 G. K. Gupta, P. Sagar, S. K. Pandey, M. Srivastava, A. K. Singh, J. Singh, A. Srivastava, S. K. Srivastava and A. Srivastava, *Nanoscale Res. Lett.*, 2021, **16**, 85.

54 A. Ahmad, M. A. Gondal, M. Hassan, R. Iqbal, S. Ullah, A. S. Alzahrani, W. A. Memon, F. Mabood and S. Melhi, *ACS Omega*, 2023, **8**, 21653–21663.

55 D. L. Vu, J. S. Seo, H. Y. Lee and J. W. Lee, *RSC Adv.*, 2017, **7**, 4144–4151.

56 Y. Liu, X. Liu, W. Dong, L. Zhang, Q. Kong and W. Wang, *Sci. Rep.*, 2017, **7**, 12437.

57 C. Julien, M. Massot, R. Baddour-Hadjean, S. Franger, S. Bach and J. P. Pereira-Ramos, *Solid State Ionics*, 2003, **159**, 345–356.

58 J. E. Post, D. A. McKeown and P. J. Heaney, *Am. Mineral.*, 2021, **106**, 351–366.

59 S. A. Elsherif, H. M. Abuzeid, A. M. Hashem and N. A. Abdel Ghany, *J. Energy Storage*, 2023, **74**, 109341.

60 X. Zhang, L. Gao, R. Guo, M. Ma and T. Hu, *Appl. Surf. Sci.*, 2022, **572**, 151458.

61 S. Thior, V. N. Kitenge, K. O. Otun, R. A. M. Adam, N. F. Diop, B. D. Ngom and N. Manyala, *New J. Chem.*, 2024, **49**, 2129–2142.

62 J. Zhao, T. Zhang, J. Ren, Z. Zhao, X. Su, W. Chen and L. Chen, *Chem. Commun.*, 2023, **59**, 2978–2981.

63 T. Zhai, S. Sun, X. Liu, C. Liang, G. Wang and H. Xia, *Adv. Mater.*, 2018, 1706640.

64 C. Zhong, Y. Deng, W. Hu, D. Sun, X. Han, J. Qiao, and J. Zhang, *Electrolytes For Electrochemical Supercapacitors*, 2016.

65 V. Ganesan and M. S. B. Kadhar Mohamed, *Chem. Eng. Res. Des.*, 2025, **220**, 635–651.

66 K. Gajewska, A. Moyseowicz, D. Minta and G. Gryglewicz, *J. Mater. Sci.*, 2023, **58**, 1721–1738.

67 D. A. Harrington, *J. Electroanal. Chem.*, 2015, **737**, 30–36.

68 N. L. Fröhlich, J. J. J. Eggebeen and M. T. M. Koper, *Electrochim. Acta*, 2024, **494**, 144456.

69 E. M. Korek, R. Teotia, D. Herbig and R. Brederlow, *Biosensors*, 2024, **14**, 241.

70 S. Skale, V. Doleček and M. Slemnik, *Corros. Sci.*, 2007, **49**, 1045–1055.

71 N. Meddings, M. Heinrich, F. Overney, J. S. Lee, V. Ruiz, E. Napolitano, S. Seitz, G. Hinds, R. Raccichini, M. Gaberšček and J. Park, *J. Power Sources*, 2020, **480**, 228742, DOI: **10.1016/j.jpowsour.2020.228742.**

72 E. Taer, D. K. H. Tampubolon, A. Apriwandi, R. Farma, R. N. Setiadi and R. Taslim, *J. Phys.: Conf. Ser.*, 2021, **2049**, 012009.

73 S. Rajeevan, S. John, D. Ponnamma and S. C. George, *J. Energy Storage*, 2022, **56**, 105919, DOI: **10.1016/j.est.2022.105919.**

74 A. Sanchez-Sanchez, M. T. Izquierdo, S. Mathieu, J. Ghanbaja, A. Celzard and V. Fierro, *J. Adv. Res.*, 2020, **22**, 85–97.

75 H. Vijeth, S. P. Ashokkumar, L. Yesappa, M. Niranjana, M. Vandana and H. Devendrappa, *RSC Adv.*, 2018, **8**, 31414–31426.

76 M. Lao, P. Li, Y. Jiang, H. Pan, S. X. Dou and W. Sun, *Nano Energy*, 2022, **98**, 107231, DOI: **10.1016/j.nanoen.2022.107231.**

77 S. J. Uke, S. P. Mardikar, D. R. Bambole, Y. Kumar and G. N. Chaudhari, *Mater. Sci. Energy Technol.*, 2020, **3**, 446–455.

78 V. Sunil, B. Pal, I. Izwan Misnon and R. Jose, *Mater. Today: Proc.*, 2020, **46**, 1588–1594.

79 W. Liu, X. Li, J. Sun, S. Zuo, C. Yao and X. Li, *J. Mater. Sci. Mater. Electron.*, 2023, **34**, 1–15.